An indirect method to calibrate the interfacial cohesive material law for FRCM-concrete joints

CrossMark

F. Focacci[a], T. D'Antino[b], C. Carloni[c,*], L.H. Sneed[d], C. Pellegrino[e]

[a] Università eCampus, Via Isimbardi 10, 22060 Novedrate, CO, Italy
[b] Politecnico di Milano, Piazza Leonardo da Vinci 32, 20133 Milan, MI, Italy
[c] University of Bologna, Viale Risorgimento 2, 40136 Bologna, BO, Italy
[d] Missouri University of Science and Technology, 1401 North Pine Street, Rolla, MO 65409, USA
[e] University of Padova, via Marzolo 9, 35131 Padova, PD, Italy

ARTICLE INFO

ABSTRACT

The cohesive material law (CML), i.e., relationship between the interfacial shear stress and slip between a fiber reinforced composite and the substrate, is a fundamental tool to model the structural behavior of composite-strengthened elements. A crucial problem that researchers working in the field of strengthening applications with fiber reinforced cementitious matrix (FRCM) composites face is how to obtain the CML. A direct method to determine the CML could be applied if the longitudinal strain is measured along the bonded length. However, since the critical interface for some FRCM composites appears to be the interface between the fibers and matrix, measuring the fiber strain in FRCM composites is a difficult task due to the presence of the matrix that embeds the fiber textile. To overcome this difficulty, an indirect method is proposed in this paper. The parameters of the CML are determined by fitting experimental data in terms of peak load measured for different composite bonded lengths. The procedure is applied to single-lap shear test results previously published by the authors. The CML obtained shows good correlation with the CML obtained from direct calibration of strain profiles measured along the bonded length and is able to predict the experimental load responses.

1. Introduction

Fiber reinforced cementitious matrix (FRCM) composites are comprised of inorganic cement-based matrices reinforced with high strength continuous fibers organized in uni- or multi-directional open textiles or fabric. FRCM composites have gained popularity in the last decade as an alternative material to fiber reinforced polymer (FRP) composites. FRCM composites can be used as externally bonded reinforcement of masonry and reinforced concrete (RC) structures. Experimental tests showed that FRCM composites are effective in flexural strengthening [1–10], shear strengthening [10–17], and confinement [18,19] of RC elements. Furthermore, they can be employed for in-plane and out-of-plane strengthening of masonry walls [20–24], and for strengthening of masonry arches and vaults [25–30].

Failure of RC and masonry elements externally strengthened with FRCM composites is usually due to the loss of composite action associated with debonding, which can occur at different interfaces [31–33] as shown in Fig. 1: 1) at the matrix-fiber interface with slippage of the fibers with respect to the matrix layers (Fig. 1a); 2) at

the matrix-fiber interface with interlaminar failure (delamination) of the composite (Fig. 1b); 3) at the FRCM-substrate interface with detachment of the entire composite strip (Fig. 1c); 4) at the FRCM-substrate interface with detachment of a thin layer of the substrate that is still attached to the FRCM strip (Fig. 1d). It should be noted that different FRCM systems commercially available may experience debonding at different interfaces. However, for the majority of the FRCM systems, when a single layer of fibers is employed, debonding occurs at the matrix-fiber interface and is characterized by slippage of the fibers with respect to the matrix [34].

The bond properties of FRCM-substrate joints have been experimentally investigated by means of single-lap shear tests [35,36], double-lap shear tests [37], or beam tests [25]. A comparison between the results of single- and double-lap shear tests performed on the same FRCM composite is discussed in [38]. A fracture mechanics approach has been used to study the debonding phenomenon in those test setups [35]. A fracture mechanics Mode-II condition is generally assumed, which implies the detachment of the composite along one of the interfaces introduced above due to the presence of shear stresses
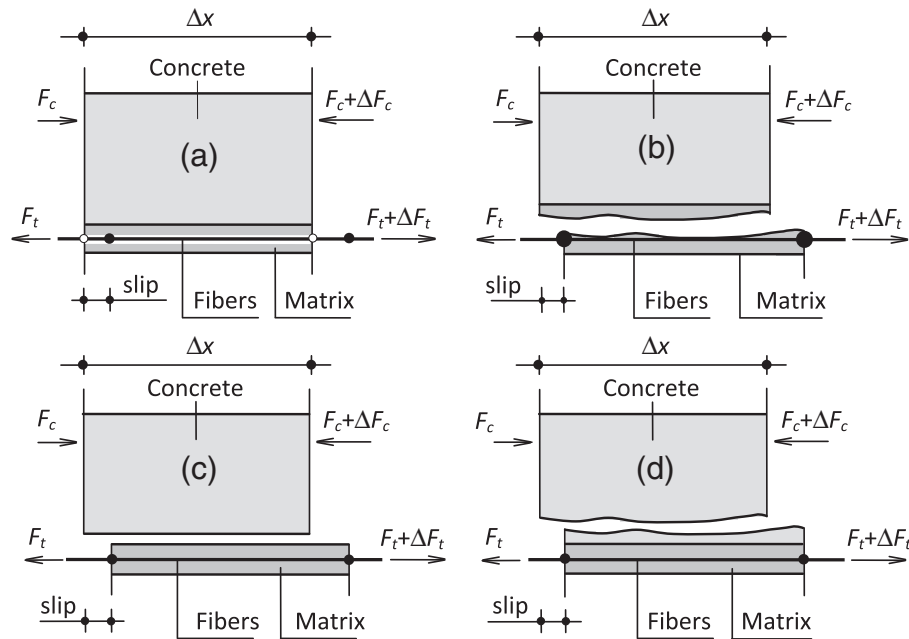
Fig. 1. Different possible debonding surfaces. F_c and F_t are the compressive resultant force acting on the concrete and the tensile force acting on the textile at a certain cross-section, respectively. ΔF_c and ΔF_t are the increments of these forces associated with the cross-section at the distance Δx.

associated with slip between the faces of the interfacial crack. To describe the debonding as a Mode-II problem, a cohesive material law (CML) is introduced that represents the relationship between the interfacial shear stress (τ) and the relative displacement or slip (s) between the faces of the crack at any location along the interface. A similar approach is used for the FRP-concrete [39,40] or FRP-masonry [41–44] interface. The key assumption behind the use of a CML is the fact that the interface is fictitiously reduced to a zero-thickness layer of material whose properties are defined by the CML itself. Once the CML is known for a certain interface, the crack initiation and propagation can be fully described. In particular, the area under the CML curve represents the fracture energy G_F that is required to advance the interfacial crack by a unit amount. G_F is related to the debonding load (DL), i.e., the maximum force that can be transferred at the interface before the onset of crack propagation. DL could be considered as the equivalent term for the bond capacity (BC), a term typically used for FRP-substrate joints. In [35], DL was termed P_{deb} to highlight that it is the load corresponding to the onset of crack propagation, but not necessarily the maximum load transferred at the FRCM-concrete joint interface. This is because the CML relationship of some FRCM composites is followed by a constant shear stress τ_f associated with any slip greater than a certain slip s_f. An effective bond length l_{eff}, defined as the minimum bonded length to reach DL (or P_{deb}) neglecting the effect of friction, is associated with the interfacial stress transfer mechanism. l_{eff} can be computed from the CML; a closed-form formula can be derived if the CML function has certain mathematical characteristics [43,44]. Otherwise, l_{eff} can be evaluated numerically.

A fundamental problem that researchers working in the field of FRCM strengthening applications face is how to obtain the CML function from laboratory tests. A direct method, employed in [45] for FRP-concrete joints, would require that the longitudinal strain is measured along the bonded length. If the fibers slip with respect to the embedding layers of matrix, fiber strains should be measured. Measuring the fiber strain in FRCM composites is a difficult task due to the presence of the matrix that embeds the fiber textile. Strain gauges can be applied to the fibers before or after casting the composite strip. In the former case, fiber bundles and strain gauges are embedded within the matrix [34–36], whereas in the latter strain gauges are applied to the fiber bundles through slots created into the matrix while

casting the composite strip [34,35]. When strain gauges are embedded within the composite, the mechanical interlocking provided by the matrix induces increasing shear stresses at the fiber-gauge interface, which eventually causes debonding of the gauges from the fibers for high values of interfacial slip. On the other hand, when gauges are applied through slots created into the matrix, stress concentration at the edges of the matrix slots could affect the strain measurements. Digital image correlation (DIC) techniques, which were effectively employed with FRP composites [46], should not be used to obtain strain profiles of FRCM composites when the fibers are covered by a matrix layer. In fact, the strain measured on the external surface of the matrix layer that covers the fibers is generally different from the fiber strain [47]. It should be noted that if the interfacial crack occurs at the FRCM-concrete interface, the strain to be measured should be within the matrix as close as possible to the concrete substrate, which would be challenging because it would require embedding strain gauges within the thickness of the matrix. Therefore, although a direct method to determine the CML is desirable, it might not be feasible for most of the FRCM systems commercially available.

A possible way to determine the CML could be to employ an indirect method based on experimental parameters that can be easily evaluated during tests. In this case, one or more CML functions, whose shape depends on several unknown parameters, must be assumed, based on researchers' experience with similar FRCM systems or FRP composites. Then, the parameters of the CML(s) should be calibrated against the experimental data, which implies that a calibration criterion is adopted. In this paper, the indirect method proposed in [37] to obtain the CML is applied to the experimental data published in [35,36]. The experimental data refer to single-lap shear tests. The FRCM tested is comprised of one layer of polyparaphenylene benzo-bisoxazole (PBO) fiber textile embedded within two layers of a polymer-modified cement-based mortar. The CML(s) obtained with the method proposed is compared with the CML obtained from direct calibration published in [35]. It should be noted that several shapes of the CML function are used in this paper to apply the indirect method, and that the method itself is not limited to specific functions. An advantage to the method proposed is that it does not require sophisticated testing and measurement techniques that some laboratories might not be able to perform. Although the method is used with single-lap shear test experimental
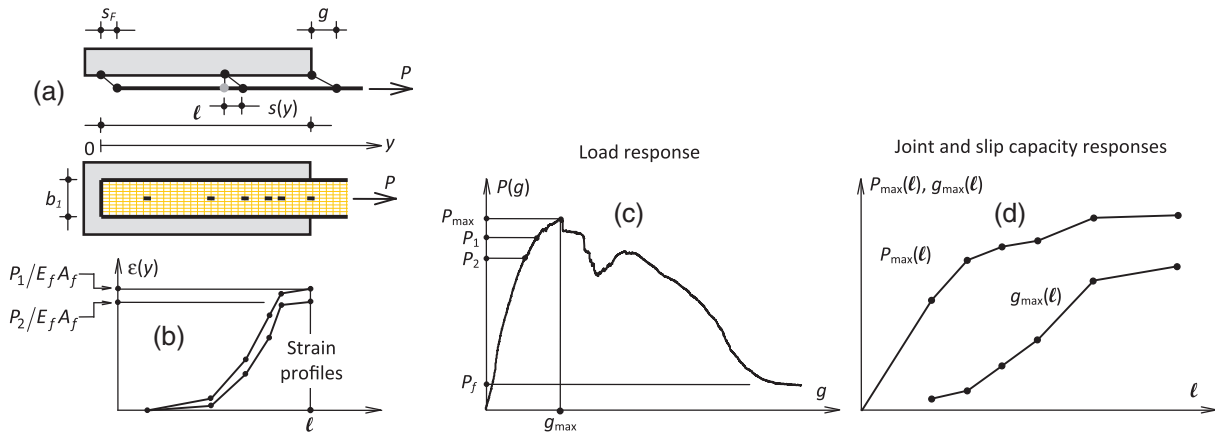
Fig. 2. (a) Sketch of a single-lap shear test. Example of: (b) experimental strain profiles, (c) experimental load response, and (d) experimental joint and slip capacity responses.

data, which is the most popular test setup among the setups mentioned above, it can be also used with experimental data obtained employing other test setups.

2. Background

Referring to Fig. 2, the experimental results of single-lap shear tests are usually expressed in terms of one or more of the following functions: i) strain profile $\varepsilon(y)$, i.e., longitudinal fiber strain on the abscissa y (Fig. 2b); ii) load response $P(g)$, i.e., plot of the applied load P versus loaded end slip g (Fig. 2c); iii) joint capacity (JC) response $P_{max}(\ell)$, i.e., plot of the peak applied load P_{max} versus bonded length ℓ (Fig. 2d); and iv) slip capacity (SLC) response $g_{max}(\ell)$, i.e., plot of the loaded end slip g_{max} corresponding to the peak load P_{max} versus bonded length ℓ (Fig. 2d). In addition, functions of the free end slip s_F (Fig. 2a) could be obtained.

The availability of the experimental $\varepsilon(y)$, $P(g)$, $P_{max}(\ell)$, and $g_{max}(\ell)$ responses depends on the adopted experimental program and test setup. Each bond test can provide many strain profiles (a strain profile for each applied load value P) and one load response, while several tests performed with different bonded lengths are needed to obtain the JC $P_{max}(\ell)$ and SLC $g_{max}(\ell)$ responses. Furthermore, the construction of the JC response $P_{max}(\ell)$ requires that all specimens included in the experimental campaign are characterized by the same bonded width b_1 (Fig. 2). Experimental results of specimens with different widths b_1 can be used to construct the JC response under the assumption that the load responses, and consequently the maximum loads, are proportional to the bonded width of the specimen (i.e., the bond behavior of the FRCM material does not exhibit a width effect [48]).

In this paper, the results of single-lap shear tests presented in [35,36] and discussed in Section 3 are considered to apply an indirect method to calibrate a CML, since the experimental work in [35,36] provides the experimental strain profiles $\varepsilon(y)$ and the $P(g)$, $P_{max}(\ell)$, and $g_{max}(\ell)$ responses. In this paper, only the $P_{max}(\ell)$ response is considered in the calibration procedure. Then, the ability of the CML, calibrated against the $P_{max}(\ell)$ response, to capture the experimental $P(g)$ and $g_{max}(\ell)$ responses is investigated. Results of tests on specimens with different bonded width b_1 were considered in [35,36] and are employed in this paper to analyze a relatively large set of experimental data. In fact, the experimental results presented in [35,36] showed that no width effect exists in the shear stress transfer between the FRCM material tested and the substrate. The absence of a width effect was confirmed by double-lap shear tests performed in [38] on the same FRCM material. The strain capacity (SC) response $\varepsilon_{max}(\ell)$, which is directly related to the JC response $P_{max}(\ell)$ by Eq. (1) for the case of linear elastic behavior of the fibers, is considered in this paper:

$$\varepsilon_{max}(\ell) = \frac{P_{max}(\ell)}{E_f A_f} \tag{1}$$

where E_f is the elastic modulus of the fibers and A_f is the cross-sectional area of the fibers in the FRCM composite. It should be noted that the experimental results selected to construct the SC response must be obtained from specimens that exhibit the same failure mode (Fig. 1).

3. Experimental results and CML based on the strain profiles

The experimental results presented in [35,36] are employed in this paper to study the feasibility of calibrating the CML of an FRCM material using an indirect method based on the SC response. Forty-two single-lap shear tests, out of the 84 tests with the same number of matrix layers and with both longitudinal and transversal fiber bundles presented in [35,36], are considered in this paper (Table 1). Only specimens that reported a (relatively) even distribution of the applied load according to a criterion proposed in [36] are considered. Specimens DS_330_43_S_1^T and DS_330_43_S_5 were also included because the CML directly obtained from the strain profile of these two specimens is in good agreement with the results herein presented. This allows for limiting the effect of the experimental uncertainties on the results obtained by the indirect calibration method proposed. The choice of the experimental work presented in [35,36] among those published in the technical literature was based on the availability of experimental results of specimens with different bonded lengths. Furthermore, a CML calibrated with a direct method based on the strain measurements is presented in [35]. This allows for comparison between the CML calibrated with a direct method and the CML calibrated with the indirect method employed.

The experimental test set-up employed in [35,36] is depicted in Fig. 3a. The specimens were comprised of a PBO FRCM composite strip bonded to the surface of a concrete prism. The PBO fibers used were in the form of an unbalanced textile with longitudinal bundles spaced at 10 mm and transversal bundles, all placed on one side of the longitudinal bundles, spaced at 20 mm. One layer of fibers was embedded within two layers of matrix only in the bonded area. Fibers were left bare outside. Aluminum plates were epoxy-bonded to the end of the bare fiber strip to improve gripping with the testing machine. Different bonded lengths ℓ, namely 100 mm, 150 mm, 200 mm, 250 mm, 330 mm, and 450 mm, were investigated. The bonded width b_1 was equal to 34 mm (4 bundles), 43 mm (5 bundles), 60 mm (7 bundles), or 80 mm (9 bundles).

The composite strips were applied to the formed faces of concrete prisms with a cross-section of 125 mm × 125 mm and a length of either 375 mm (for bonded lengths up to 330 mm) or 510 mm (for bonded length equal to 450 mm). A linear variable displacement transducer (LVDT) was mounted on the concrete surface on either side of the

Table 1
Specimens considered for the calibration of the CML.

Specimen	ℓ [mm]	b_1 [mm]	b_f [mm]	A_f [mm²]	P_{max} [kN]	σ_{max} [MPa]	ε_{max} [%]	g_{max} [mm]	Avg. ε_{max} [%]	Avg. g_{max} [mm]
DS_100_60_1	100	60	70	3.22	3.69	1150	0.556	0.100	0.57	0.207
DS_100_60_2				3.22	3.83	1190	0.577	0.235		
DS_100_60_3				3.22	3.77	1170	0.568	0.286		
DS_150_60_1	150	60	70	3.22	5.25	1630	0.791	0.301	0.78	0.339
DS_150_60_2				3.22	5.04	1570	0.760	0.376		
DS_200_34_1	200	34	40	1.84	3.05	1660	0.805	0.380	0.85	0.756
DS_200_34_3				1.84	3.44	1870	0.908	0.398		
DS_200_60_2		60	70	3.22	5.66	1760	0.853	1.156		
DS_200_60_3				3.22	5.44	1690	0.820	1.090		
DS_250_34_3^T	250	34	40	1.84	2.82	1530	0.744	1.463	0.88	1.171
DS_250_34_5				1.84	2.89	1570	0.762	1.360		
DS_250_34_6				1.84	3.61	1960	0.952	1.250		
DS_250_60_1		60	70	3.22	6.68	2070	1.007	0.590		
DS_250_60_2				3.22	6.17	1920	0.930	1.731		
DS_250_60_3				3.22	5.70	1770	0.859	0.631		
DS_330_43_S_1^T	330	43	50	2.30	4.48	1950	0.946	3.375	0.99	2.142
DS_330_43_S_2^T				2.30	5.12	2230	1.081	2.652		
DS_330_43_S_5				2.30	4.03	1750	0.853	2.177		
DS_330_60_2^T		60	70	3.22	6.56	2040	0.989	2.312		
DS_330_60_3^T				3.22	6.06	1880	0.914	1.313		
DS_330_60_4^T				3.22	6.50	2020	0.980	1.713		
DS_330_60_D_3				3.22	6.56	2040	0.989	2.674		
DS_330_60_D_5				3.22	6.69	2080	1.009	2.452		
DS_330_60_S_2				3.22	7.31	2270	1.102	1.287		
DS_330_60_S_3				3.22	6.55	2030	0.987	2.410		
DS_330_80_D_1		80	90	4.14	8.90	2150	1.044	2.934		
DS_330_80_D_2				4.14	8.68	2100	1.019	0.745		
DS_330_80_D_4				4.14	8.42	2030	0.987	2.113		
DS_330_80_D_5				4.14	8.58	2070	1.006	1.833		
DS_450_60_1	450	60	70	3.22	6.40	1990	0.965	1.940	1.01	2.369
DS_450_60_2				3.22	6.34	1970	0.956	3.590		
DS_450_60_4				3.22	5.77	1790	0.870	2.566		
DS_450_60_5				3.22	6.51	2020	0.981	2.063		
DS_450_60_6				3.22	6.79	2110	1.024	1.364		
DS_450_60_7				3.22	6.65	2060	1.003	2.684		
DS_450_60_D_1				3.22	7.01	2180	1.057	2.493		
DS_450_60_D_2				3.22	6.67	2070	1.006	2.100		
DS_450_60_D_3				3.22	7.33	2270	1.105	2.463		
DS_450_60_S_1				3.22	6.63	2060	1.000	2.330		
DS_450_60_S_2				3.22	6.86	2130	1.034	3.915		
DS_450_80_1		80	90	4.14	8.62	2080	1.011	2.344		
DS_450_80_2				4.14	9.07	2190	1.064	0.943		

composite strip near the loaded end and reacted off of a thin aluminum Ω-shaped plate attached to the bare fibers just outside the bonded area. The average of the two LVDT measurements, which is defined as global slip and assumed equal to the loaded end slip g in this paper, was used to control the tests that were conducted at a constant rate of 0.00084 mm/s. Specimens are named following the notation DS_X_Y_ (S or D)_Z$^{(T)}$, where X is the bonded length ℓ (in mm), Y is the bonded width b_1 (in mm), S (if present) indicates that strain gauges were

mounted on the specimen, D (if present) indicates that the test was conducted until a constant applied load value due to friction only was attained, Z is the specimen number, and superscript T (if present) indicates that the fiber net was oriented such that the transversal fiber bundles were placed toward the concrete prism. All specimens were comprised of a single layer of fiber textile with equivalent thickness $t_f = 0.046$ mm. The elastic modulus $E_f = 206$ GPa of the textile in the longitudinal direction was determined from tensile tests of the bare
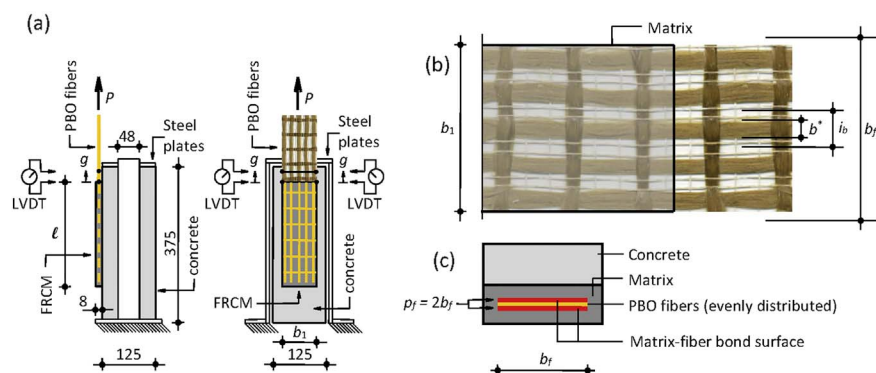
Fig. 3. (a) Front and lateral views of the experimental test setup. (b) Definition of the geometrical characteristics of the PBO textile. (c) Width p_f of the fiber-matrix bond surface adopted in this paper.

fiber bundles in [35].

Fiber strains were experimentally measured for certain specimens (indicated in Table 1 with an S before the specimen number) using strain gauges mounted on the central fiber bundle along the bonded length. The strains obtained were fitted using an analytical equation that takes into account the presence of friction at the fiber-matrix interface after debonding occurs:

$$\varepsilon(y) = \varepsilon_0 + \frac{\alpha + ky}{1 + e^{-\left(\frac{y - y_0}{\beta}\right)}} \tag{2}$$

where ε_0, α, β, and y_0 were determined using nonlinear regression analysis of the measured strain profile, and $k = 2\tau_f/(E_f t_f)$ depends on the friction contribution [35]. The CML function obtained by integration and differentiation of Eq. (2) will be named 0_CML in this paper. Four different CMLs, evaluated at four points of the load response around the assumed debonding load (DL) value, were obtained for each specimen equipped with strain gauges. An *average* CML characteristic of the specimen considered was obtained by averaging the shear stress values of the four CMLs for the same slip value. An analogous procedure was employed to average the CMLs characteristic of each specimen equipped with strain gauges to obtain the CML that is representative of all specimens considered in this paper.

Referring to Fig. 3b, different geometrical parameters are used in this paper than in [35,36] to describe the geometry of the textile. In particular, in [35,36] the textile is considered as comprised of discrete fibers bundles in the longitudinal direction with a center-to-center spacing $i_b = 10$ mm with thickness $t^* = 0.092$ mm and width $b^* = 5$ mm. Consequently, the cross sectional area of the fibers and the width of the interfacial surface are $A_f = nb^*t^*$ and $p_f^* = 2nb^*$, respectively, where n is the number of longitudinal bundles, and the coefficient 2 is introduced to account for the internal (concrete side) and external (free side) fiber-matrix interface surfaces. Furthermore, in [35,36] b_1 denotes the bonded width of the matrix (Fig. 3b). In this paper, following the approach used in [37], the fibers are considered uniformly spread within a width b_f, which is a multiple of the spacing i_b. Consequently, the cross-sectional area of the fibers and the width of the interfacial surface are $A_f = b_f t_f$ and $p_f = 2b_f$, respectively (Fig. 3c), where $t_f = 0.046$ mm is the equivalent thickness of the textile corresponding to the longitudinal fibers, defined as $t_f = p_L/\gamma_{PBO}$, where p_L is the weight of the longitudinal fibers per unit surface of the textile, and γ_{PBO} is the PBO fiber density. Consequently, $A_f = b_f t_f = nb^*t^*$, and $p_f = 2ni_b = p_f^* i_b/b^*$.

4. CML functions adopted

In this paper, five CML functions are considered for the indirect calibration to investigate the effectiveness of the proposed procedure without assuming a unique shape of the CML. The reason for choosing different CML functions is justified by the fact that the shape of the calibrated CML is unknown a-priori. Therefore, the adoption of different CML functions allows to explore the ability of a wide set of CML shapes to reproduce the experimental data. Furthermore, it allows to evaluate the robustness of the proposed method and to establish the best CML function to be adopted for the analytical modeling of the shear stress transfer phenomenon of the PBO-FRCM material tested in [35,36]. Each CML function contains several unknown parameters that were determined according to the calibration procedure described in Section 5. Since it was observed in [35,36] that the load responses of the specimens reported in Table 1 are characterized by a residual force due to the presence of a constant friction (interlocking) shear stress at the fiber-matrix interface (P_f in Fig. 2), all CMLs herein considered are followed by a constant shear stress (friction) τ_f for any slip greater than a certain slip s_f (Fig. 4). Should a different set of experimental data be used, the CML function must be chosen based on the experimental evidence. The entire relation between the slip s and the corresponding

shear stress τ will be denoted with $\tau(s)$ herein. The $\tau(s)$ relation is comprised of the CML for values of s up to s_f, and the friction shear stress τ_f for values of s larger than s_f. The analytical expression of the $\tau(s)$ relation will be named as CML even though it includes the friction shear stress.

The first CML function, named 1_CML, is derived from the expression proposed in [37] by adding a constant friction shear stress τ_f:

$$\tau(s) = \begin{cases} [\tau_0 + A(e^{-\alpha s} - e^{-\beta s})] \cdot \left(1 - \frac{s}{s_f}\right) + \tau_f & \text{if } s \leq s_f \\ \tau_f & \text{if } s > s_f \end{cases} \tag{3}$$

The set of unknown parameters is $\mathbf{p} = [\tau_0, A, \alpha, \beta, s_f, \tau_f]$. Eq. (3) represents a CML characterized by nonzero shear stress at $s = 0$ ($\tau(0) = \tau_0 + \tau_f$), followed by a constant shear stress, equal to τ_f, for $s \geq s_f$.

The second CML function, named 2_CML, is also derived from the expression proposed in [37] and is defined as:

$$\tau(s) = \begin{cases} [\tau_0 + A(e^{-\alpha s} - e^{-\beta s})] \cdot \left(1 - \frac{s}{s_0}\right) & \text{if } s \leq s_f \\ \tau_f & \text{if } s > s_f \end{cases} \tag{4}$$

In this case, the set of unknown parameters is $\mathbf{p} = [\tau_0, A, \alpha, \beta, s_0, s_f]$; τ_f is not included in $\mathbf{p}$, since continuity of the CML requires:

$$\tau_f = [\tau_0 + A(e^{-\alpha s_f} - e^{-\beta s_f})] \cdot \left(1 - \frac{s_f}{s_0}\right) \tag{5}$$

Eq. (4) represents a CML characterized by nonzero shear stress at $s = 0$ ($\tau(0) = \tau_0$), followed by a constant shear stress, equal to τ_f, for $s \geq s_f$. $s_0 \geq s_f$ must be enforced during the application of the calibration procedure in order to obtain $\tau_f \geq 0$.

The third CML function, named 3_CML, is derived from the expression proposed in [49,50] by adding a constant friction shear stress τ_f:

$$\tau(s) = A \cdot (e^{-\alpha s} - e^{-2\alpha s}) + \tau_f \tag{6}$$

In this case, the set of unknown parameters is $\mathbf{p} = [A, \alpha, \tau_f]$. Eq. (6) represents a CML characterized by a nonzero shear stress at $s = 0$ ($\tau(0) = \tau_f$). A constant shear stress, equal to τ_f, is reached when $s \rightarrow +\infty$. Thus, in this case $s_f \rightarrow +\infty$.

The fourth CML function, named 4_CML, is also derived by the expression proposed in [49,50] and is defined by:

$$\tau(s) = \begin{cases} A \cdot (e^{-\alpha s} - e^{-2\alpha s}) & \text{if } s \leq s_f \\ \tau_f & \text{if } s > s_f \end{cases} \tag{7}$$

In this case, the set of unknown parameters is $\mathbf{p} = [A, \alpha, s_f]$; τ_f is not included in $\mathbf{p}$, since continuity of the CML requires:

$$\tau_f = A(e^{-\alpha s_f} - e^{-2\alpha s_f}) \tag{8}$$

Eq. (7) represents a CML characterized by shear stress equal to zero at $s = 0$ ($\tau(0) = 0$), followed by a constant shear stress, equal to τ_f, for $s \geq s_f$.

Finally, the fifth CML function, named 5_CML, is defined as:

$$\tau(s) = A \cdot (e^{-\alpha s} \sin(\beta s - \delta) + \sin(\delta)) + \tau_0 \tag{9}$$

In this case, the set of unknown parameters is $\mathbf{p} = [A, \alpha, \beta, \delta, \tau_0]$. Eq. (9) represents a CML characterized by nonzero shear stress at $s = 0$ ($\tau(0) = \tau_0$). A constant shear stress, equal to $\tau_f = \tau_0 + A \sin \delta$, is reached when $s \rightarrow +\infty$. Thus, in this case $s_f \rightarrow +\infty$.

In the remainder of this paper, the CML functions will be named X_CML (X = 1, 2, …5).

5. Calibration method and construction of the analytical SC response $\varepsilon_{max}(\ell)$

In this section, a general overview of the calibration method is presented together with the necessary mathematical tools required to
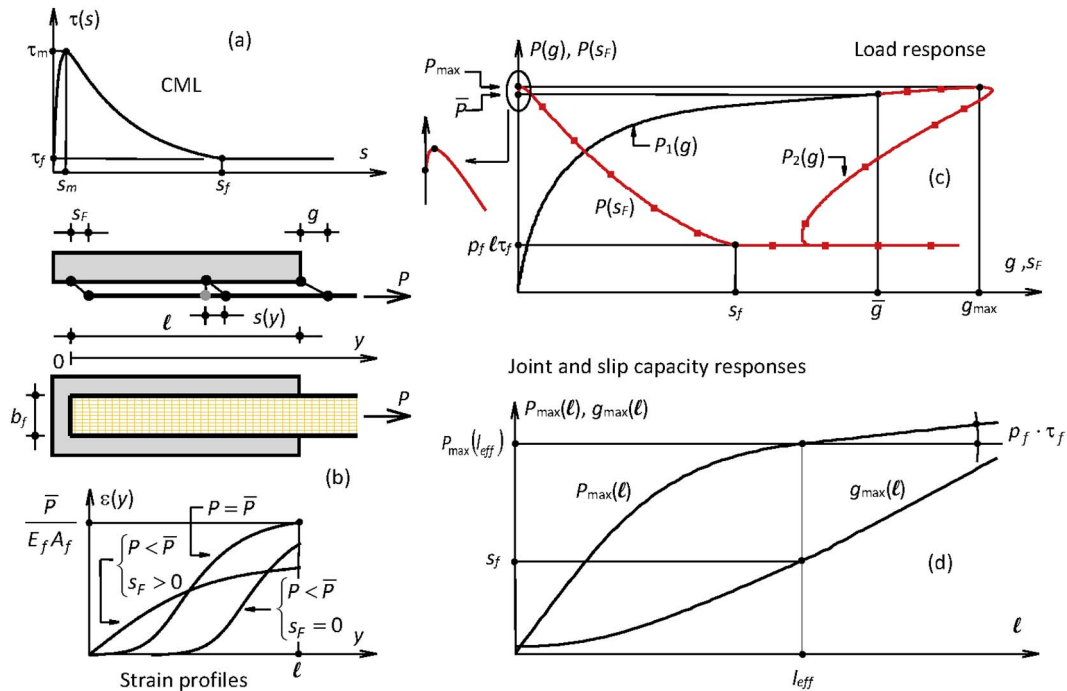
Fig. 4. (a) Typical CML for an FRCM composite. (b) Strain profiles consequent to the typical CML. (c) Load response corresponding to the typical CML. (d) Joint and slip capacity responses corresponding to the typical CML.

calibrate the X_CML. The method proposed herein is based on the experimental $\varepsilon_{max}(\ell)$ curve (i.e., the $P_{max}(\ell)$ curve divided by the axial stiffness $E_f A_f$ of the textile per Eq. 1). Once the experimental $\varepsilon_{max}(\ell)$ curve is selected, a best fitting procedure is used to calibrate the X_CML against the experimental data. This step requires that the $\varepsilon_{max}(\ell)$ curve corresponding to a certain set **p** of parameters is obtained by solving the fundamental differential equation that describes the Mode-II debonding phenomenon [43,44]. The best fitting procedure entails for the definition of a calibration criterion that is specific for the $\varepsilon_{max}(\ell)$ curve. The calibration criterion should minimize the distance between the experimental curve and the analytical curve (discussed further in Section 6.2). It should be noted that, since the entire CML is exploited to attain the peak load (at least for specimens with ℓ greater than l_{eff}), the descending branch of the experimental load responses does not need to be considered and does not limit the extension of the associated CML.

5.1. Construction of the analytical responses

The CML allows for the analytical or numerical evaluation of the strain profiles $\varepsilon(y)$, load response $P(g)$, JC response $P_{max}(\ell)$, and SLC response $g_{max}(\ell)$. The term *analytical* will be used for the strain profile and the other responses obtained from the CML, even though numerical methods have been used for the solution of the differential equations and integrals herein presented. Fig. 4 shows an idealized CML for an FRCM material and the associated relations $\varepsilon(y)$, $P(g)$, $P_{max}(\ell)$, and $g_{max}(\ell)$ for a relatively long bonded length [43,44]. The analytical responses associated with an assigned CML are determined by solving the differential equation [43,44]:

$$\frac{d^2s}{dy^2} = \frac{p_f}{E_f A_f}\tau(s) \tag{10}$$

where $s = s(y)$ is the slip at location y (Fig. 4). Boundary conditions must be enforced, for example, at the free end ($y = 0$, Fig. 4).

5.1.1. Construction of the strain profiles
The strain profile associated with the applied load P is defined by:

$$\varepsilon(y) = \frac{d}{dy}s(y) \tag{11}$$

where $s(y)$ is a solution of Eq. (10) satisfying the condition (Fig. 4b):

$$E_f A_f \left.\frac{ds}{dy}\right|_{y=\ell} = P \tag{12}$$

If the CML is followed by a constant shear stress τ_f ($s \geq s_f$, Fig. 4a), when the loaded end slip g is greater than s_f a portion of the strain profile near the loaded end presents a constant slope:

$$\frac{d\varepsilon}{dy} = \tau_f \frac{p_f}{E_f A_f} \tag{13}$$

This is a peculiarity of some FRCM materials such as the one herein investigated [35]. For FRP composites, the shear stress is generally assumed equal to zero for slips greater than a certain slip s_f. Consequently, in the case of FRP composites, the strain profiles are constant near the loaded end for $g \geq s_f$.

5.1.2. Construction of the load response
A procedure to construct the load response $P(g)$ was employed in [37] to characterize the bond properties of FRCM materials. A similar procedure is adopted herein and takes into account that the $P(g)$ response is comprised of two branches: the first branch, named $P_1(g)$, corresponds to null slips s_F at the free end (Fig. 4a,c), while the second branch, named $P_2(g)$, corresponds to nonzero slips s_F at the free end (Fig. 4c). The procedure consists of the following steps.

Step 1: evaluation of the applied force $\overline{P}$ and consequent loaded end slip $\overline{g}$ at the onset of nonzero slip at the free end. These parameters can be determined by solving Eq. (10) with the boundary conditions enforced at the free end ($y = 0$, Fig. 4):

$$\begin{cases} s(0) = 0 \\ \varepsilon(0) = \left.\frac{ds}{dy}\right|_{y=0} = 0 \end{cases} \tag{14a,b}$$

The force $\overline{P}$ and the loaded end slip $\overline{g}$ are then determined as:

$$\bar{g} = \bar{s}(\ell)$$
$$\bar{P} = E_f A_f \frac{d\bar{s}}{dy}\Big|_{y=\ell} \qquad (15a,b)$$

where $\bar{s}(y)$ is the solution of Eq. (10) with the boundary conditions in Eq. (14a,b).

Step 2: determination of the first branch $P_1(g)$ of the $P(g)$ response. $P_1(g)$ is obtained from Eq. (16):

$$g = s(\ell)$$
$$P_1(g) = \sqrt{2p_f E_f A_f \int_0^g \tau(s)ds} \qquad (16a,b)$$

Step 3: determination of the second branch $P_2(g)$ of the $P(g)$ response. $P_2(g)$ is determined by considering a set of values of the free end slip s_F and solving Eq. (10) with boundary conditions:

$$\begin{cases} s(0) = s_F \\ \varepsilon(0) = \frac{ds}{dy}\Big|_{y=0} = 0 \end{cases} \qquad (17a,b)$$

The solutions $s(y) = s_{sF}(y)$ of Eq. (10) with the boundary conditions in Eq. (17a,b) allows for associating the applied load P and loaded end slip g with each value of the free end slip s_F:

$$g(s_F) = s_{sF}(\ell)$$
$$P(s_F) = E_f E_f \frac{ds_{sF}}{dy}\Big|_{y=\ell} \qquad (18a,b)$$

The subscript sF in Eq. (18a,b) indicates that the corresponding slip profile $s_{sF}(y)$ is associated with a certain slip s_F at the free end. Hence, for each value of the parameter s_F the slip profile $s_{sF}(y)$ is determined. Consequently, for each value of s_F the loaded end slip $g(s_F)$ and the applied force $P(s_F)$ are computed. The second branch $P_2(g)$ of the $P(g)$ response is obtained by eliminating the parameter s_F between functions $P(s_F)$ and $g(s_F)$.

Step 4: determination of the $P(g)$ response. Finally, the entire $P(g)$ response is the union of branches $P_1(g)$ and $P_2(g)$, as shown in Fig. 4c. It is worth noting that the existence of both branches $P_1(g)$ and $P_2(g)$ depends on the shape of the adopted CML: the first branch does not exist, i.e., $\bar{P} = 0$, for a CML characterized by $\tau(0) = 0$ and finite derivative at $s = 0$, as observed in [43,44]. Fig. 4c shows the shape of the load response and also the relation $P(s_F)$ consequent to the typical CML represented in the same figure.

5.1.3. Construction of the strain and slip capacity responses

The SC $\varepsilon_{max}(\ell)$ and SLC $g_{max}(\ell)$ responses are determined by considering different values of the bonded length ℓ. For each value of ℓ, the load response $P(g)$ is determined applying the procedure described in the previous paragraph. Thus, the maximum load $P_{max}(\ell) = \max\{P(g)\}$ and the corresponding slip $g_{max}(\ell)$ such that $P(g_{max}(\ell)) = P_{max}(\ell)$ can be associated with each bonded length ℓ (Fig. 4d). The SC $\varepsilon_{max}(\ell)$ is then related to the JC $P_{max}(\ell)$ by Eq. (1). It should be noted that if the shear stress τ is constant and equal to τ_f for $s \geq s_f$ (see Fig. 4a), a certain bonded length l_{eff} (effective bond length) will exist such that if ℓ_1 and ℓ_2 are greater than or equal to l_{eff}:

$$P_{max}(\ell_2) = P_{max}(\ell_1) + (\ell_2 - \ell_1)\cdot p_f\cdot\tau_f \qquad (19)$$

where $P_{max}(\ell_1)$ and $P_{max}(\ell_2)$ are the maximum loads associated with the bonded lengths ℓ_1 and ℓ_2, respectively. Furthermore, depending on the shape of the initial branch of the CML and the value of τ_f, the maximum load corresponding to a certain bonded length ℓ could be attained in the second branch $P_2(g)$ of the load response, as shown in Fig. 4. In particular, this scenario occurs if the CML is such that the friction shear stress τ_f is greater than the initial shear stress $\tau(0)$. As mentioned previously, this is a peculiarity of certain FRCM materials, since in the case of the FRP composites the shear stress is zero for slips greater than a certain slip s_f. Consequently, in the case of the FRP composites, the

bond capacity coincides with the maximum load for bonded lengths ℓ greater than the effective bond length l_{eff}^{FRP}.

The analytical load response $P(g)$, SC response $\varepsilon_{max}(\ell)$, and SLC response $g_{max}(\ell)$ determined from a CML depend on the set **p** of parameters that define the shape of the CML itself. Therefore, in the remainder of the paper the load, SC, and SLC responses will be named $P_\mathbf{p}(g)$, $\varepsilon_{max,\mathbf{p}}(\ell)$, and $g_{max,\mathbf{p}}(\ell)$, respectively, to avoid confusion with the companion experimental responses.

5.2. Calibration criterion

Once a CML $\tau(s)$ defined by a set **p** of unknown parameters is considered, the set **p** of values of the unknown parameters that provides the best fit between the analytical and experimental results can be determined by minimizing the distance between the experimental and the companion analytical responses. In this paper, the criterion of minimizing the distance between the experimental and analytical data is applied to the $\varepsilon_{max}(\ell)$ response. Thus, the set **p** is determined as the set of parameters that minimizes the distance between $\varepsilon_{max,\mathbf{p}}(\ell)$ and $\varepsilon_{max}(\ell)$:

$$d(\varepsilon_{max}(\ell),\varepsilon_{max,\mathbf{p}}(\ell)) \leq d(\varepsilon_{max}(\ell),\varepsilon_{max,\mathbf{p}}(\ell)) \quad \forall \ \mathbf{p} \qquad (20)$$

where $d(\varepsilon_{max}(\ell),\varepsilon_{max,\mathbf{p}}(\ell))$ is the distance between the experimental $\varepsilon_{max}(\ell)$ and analytical $\varepsilon_{max,\mathbf{p}}(\ell)$ responses determined as:

$$d(\varepsilon_{max}(\ell),\varepsilon_{max,\mathbf{p}}(\ell)) = \sum_{j=1}^{N} [\varepsilon_{max,j} - \varepsilon_{max,\mathbf{p}}(\ell_j)]^2 \qquad (21)$$

where N is the number of bonded lengths $\ell_1, \ell_2, \ldots, \ell_N$ investigated during the experimental campaign, and $\varepsilon_{max,j}$ $(j = 1, 2, \ldots N)$ is the average maximum strain of all specimens having bonded lengths ℓ_j. In this paper, $N = 6$, since six different bonded lengths ranging from 100 mm to 450 mm were considered (Section 3). Table 1 provides the average maximum strain $\varepsilon_{max,j}$ for each bonded length.

The friction shear stress τ_f can be regarded as an element of the set **p** of unknown parameters, or it can be evaluated directly on the basis of the constant load P_f measured in the final branch of certain experimental load responses as (Fig. 2, Fig. 4):

$$\tau_f = \frac{P_f}{\ell p_f} \qquad (22)$$

6. Results and discussion

6.1. Calibrated CML functions

The application of the calibration criterion discussed in Section 5.2 allows the determination of one CML for each of the five expressions given in Eqs. (3), (4), (6), (7), and (9). These CMLs are named X_CML-PL to designate that they have been calibrated against the experimental response $\varepsilon_{max}(\ell)$ (which is related to the $P_{max}(\ell)$ response via Eq. (1)). The CML associated with the 0_CML expression calibrated against the strain profiles is named 0_CML-sp.

As mentioned in Section 5.2, the friction shear stress τ_f can be regarded as an element of the set **p** of unknown parameters, or it can be evaluated directly if P_f is measured in the final branch of the experimental load responses. In this section, with the exclusion of the 5_CML equation, two sets of parameters **p** were determined for each X_CML-PL: the first set includes the friction shear stress τ_f as one of the calibrated parameters, while the second set does not, and $\tau_f = 0.03$ MPa is adopted. The value of τ_f was determined applying Eq. (22) for specimens that were tested until a constant applied load value due to friction only was attained (Section 3). $\tau3$ at the end of the name of the CML is used to indicate that the set of parameters **p** does not include τ_f. For example, 1_CML-PL-$\tau3$ is the CML determined using function 1_CML calibrated against the experimental response $\varepsilon_{max}(\ell)$, with
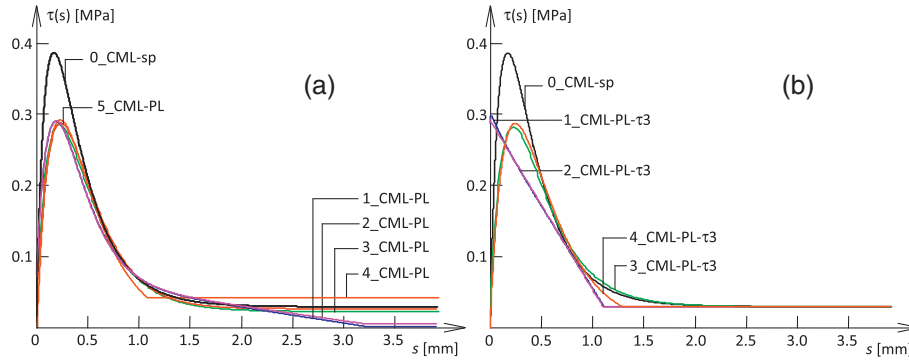
Fig. 5. (a) Comparison of X_CML-PL determined by Eqs. (3), (4), (6), (7), and (9) and calibration criterion. (b) Comparison of X_CML-PL-τ3 determined by Eqs. (3), (4), (6), (7), and (9) and calibration criterion. Each plot includes the 0_CML-sp relation for comparison.

$\tau_f = 0.03$ MPa.

The CMLs associated with Eqs. (3), (4), (6), (7), and (9) and calibrated using the aforementioned criterion are shown in Fig. 5. Fig. 5 also shows the 0_CML-sp curve obtained from the fitting of the strain profiles [35,36]. It should be noted that the ordinates of the 0_CML-sp curve shown in Fig. 5 are different from those of the CML reported in [35] due to the different (although equivalent) values of the width of the fiber-matrix interface surface as mentioned in Section 3. Table 2 summarizes the main parameters characterizing the shape of the CMLs obtained with the proposed calibration criterion. Symbols adopted in Table 2 are defined in Fig. 2, and the fracture energy G_F is given by:

$$G_F = \int_0^{s_f} \tau(s)\,\mathrm{d}s \tag{23}$$

For some CMLs adopted, G_F is not reported in Table 2 because, since the shear stress approaches asymptotically the friction shear stress τ_f, the fracture energy computed as the area under the curve in the range $[0, s_f]$ approaches infinity.

Fig. 5 shows that the CML derived by the strain profiles and the X_CMLs calibrated against the experimental strain capacity response have similar shapes (with exception of the 1_CML-PL-τ3 and the 2_CML-PL-τ3 relations), although the 0_CML-sp relation provides higher peak shear stress. This difference may be due to the fact that the 0_CML-sp was developed for points of the load response close to the DL P_{deb} and only for specimens with bonded length greater than or equal to 330 mm, while the X_CMLs were obtained from the experimental results of all specimens summarized in Table 1. Fig. 5 and Table 2 show that Eqs. (3), (4), (6), (7), and (9) and the proposed calibration criterion provide CMLs characterized by similar values of the maximum shear stress τ_m and (with the exception of the 1_CML-PL-τ3 and 2_CML-PL-τ3 relations) corresponding slip s_m. τ_m ranges between 0.28 MPa and 0.30 MPa, and s_m ranges between 0.19 mm and 0.25 mm. Differences can be observed among the descending branches of the CMLs. In

particular, Fig. 5a shows that lower friction shear stress τ_f is associated with the 1,2_CML-PL relations (Eqs. (3) and (4), respectively) as compared to the 3,4,5_CML-PL relations (Eqs. (6), (7), and (9), respectively). This observation is related to the different analytical expressions of the CMLs. The 3,4,5_CML-PL relations provide friction shear stress τ_f of the same order of magnitude of $\tau_f = 0.03$ MPa evaluated on the basis of the load P_f on the experimental load responses.

6.2. Comparison of the analytical and experimental responses

Once the CML is calibrated against the experimental SC response $\varepsilon_{\max}(\ell)$, the same CML can be employed to construct the strain profiles $\varepsilon(y)$, the load response $P(g)$, and the SLC response $g_{\max}(\ell)$. Similarly, the CML calibrated against the experimental strain profiles $\varepsilon(y)$ can be employed to construct the $P(g)$, $\varepsilon_{\max}(\ell)$, and $g_{\max}(\ell)$ responses. Then, the distance between the experimental and analytical responses can be evaluated to determine the ability of the calibrated CML to capture the remaining experimental data. In particular, the ability of a CML defined by a certain set of parameters **p** to capture the experimental results in terms of $P(g)$, $\varepsilon_{\max}(\ell)$, and $g_{\max}(\ell)$ responses is evaluated as follows.

The authors propose the parameter defined in Eq. (24) to evaluate the approximation of the experimental load response $P(g)$ of the generic K-th specimen ($K = 1, 2, \dots, m$) of the $m = 42$ specimens tested by the response $P_\mathbf{p}(g)$:

$$E_{PK}\mathbf{p} = \frac{\sqrt{\sum_{j=1}^{n_K}[P_j - P_\mathbf{p}g_j]^2}}{P_{n_K}} \tag{24}$$

where $g_1, g_2, \dots, g_{n_K}$ are the values of slip enforced at the loaded end of the K-th specimen, and $P_1, P_2, \dots, P_{n_K}$ are the corresponding applied loads. Eq. (24) was applied to the ascending branches of the experimental $P(g)$ responses only, since the tests discussed in [35,36] were performed under loaded end displacement control, and consequently they did not allow the snap-back phenomenon (Fig. 4c) to be captured. Thus, P_{n_K} is the maximum load $P_{\max}$ applied to the K-th specimen. The subscript K in Eq. (24) indicates that the experimental response of a generic K-th specimen is considered. Consequently, m values of E_{PK} are obtained with Eq. (24) for each set **p**. The average of the value of E_{PK} defined as:

$$E_P(\mathbf{p}) = \frac{1}{m} \cdot \sum_{K=1}^{m} E_{PK}(\mathbf{p}) \tag{25}$$

will be used to evaluate the overall ability of the CML defined by the set **p** to capture the experimental $P(g)$ responses of the m tested specimens.

Similar to the procedure above, the parameter that evaluates the approximation of the experimental SC response $\varepsilon_{\max}(\ell)$ by the response $\varepsilon_{\max,\mathbf{p}}(\ell)$ is defined as:

Table 2
Main parameters characterizing the CMLs obtained with the procedure based on the $\varepsilon_{\max}(\ell)$ response.

CML	τ_m [MPa]	s_m [mm]	τ_f [MPa]	s_f [mm]	G_F [N/mm]
1_CML-PL	0.29	0.20	0.00	3.25	0.24
2_CML-PL	0.29	0.19	0.01	3.21	0.24
3_CML-PL	0.29	0.22	0.02	$\rightarrow +\infty$	–
4_CML-PL	0.29	0.23	0.04	1.10	0.18
5_CML-PL	0.29	0.23	0.03	$\rightarrow +\infty$	–
1_CML-PL-τ3	0.30	0.01	0.03	1.11	0.18
2_CML-PL-τ3	0.29	0.00	0.03	1.11	0.18
3_CML-PL-τ3	0.28	0.22	0.03	$\rightarrow +\infty$	–
4_CML-PL-τ3	0.29	0.25	0.03	1.29	0.19

Table 3
Values of parameters associated with approximation of the experimental responses with the analytical responses relative to the X_CMLs with the parameters **p**.

CML	$E_\varepsilon(\mathbf{p})$	$E_g(\mathbf{p})$	$E_P(\mathbf{p})$
1_CML-PL	0.047	0.368	10.922
2_CML-PL	0.046	0.405	10.576
3_CML-PL	0.052	0.460	11.234
4_CML-PL	0.071	0.468	10.923
5_CML-PL	0.053	0.465	11.647
1_CML-PL-τ3	0.054	0.495	12.862
2_CML-PL-τ3	0.056	0.494	12.686
3_CML-PL-τ3	0.066	0.474	10.024
4_CML-PL-τ3	0.055	0.460	12.001
0_CML-sp	0.295	0.722	10.933

$$E_\varepsilon(\mathbf{p}) = \frac{\sqrt{\sum_{j=1}^{N}[\varepsilon_{max,j} - \varepsilon_{max,\mathbf{p}}(\ell_j)]^2}}{\varepsilon_{max,N}} \quad (26)$$

The parameter that estimates the approximation of the experimental SLC response $g_{max}(\ell)$ by the response $g_{max,\mathbf{p}}(\ell)$ is defined as:

$$E_g(\mathbf{p}) = \frac{\sqrt{\sum_{j=1}^{N}[g_{max,j} - g_{max,\mathbf{p}}(\ell_j)]^2}}{g_{max,N}} \quad (27)$$

where $g_{max,j}$ is the average loaded end slip at maximum load of all specimens having bonded length ℓ_j, as shown in Table 1.

Table 3 summarizes the values of $E_P(\mathbf{p})$, $E_\varepsilon(\mathbf{p})$, and $E_g(\mathbf{p})$ corresponding to the approximation of the experimental responses with the analytical responses for each CML. Among the CMLs calibrated against the $\varepsilon_{max}(\ell)$ responses for which τ_f has been included in **p** (see Fig. 5a), Table 3 shows that 2_CML-PL (Eq. (4)) provides the best result in terms of strain capacity (lowest value of $E_\varepsilon(\mathbf{p})$). Nonetheless, very similar CMLs and $E_\varepsilon(\mathbf{p})$ values were obtained with all the X-CML-PL equations. 2_CML-PL also provides the best result in terms of reproducing the load responses $P(g)$ of the m specimens (lowest value of $E_P(\mathbf{p})$).

In Fig. 6 the experimental responses $\varepsilon_{max}(\ell)$ and $g_{max}(\ell)$ are compared with the corresponding analytical responses associated with 2_CML-PL. In particular, Fig. 6a shows the plot of the 2_CML-PL relation

and the corresponding parameters. Fig. 6b shows that the SC response associated with 2_CML-PL provides a good approximation of the experimental SC response. Fig. 6c shows that the analytical SLC response $g_{max,\mathbf{p}}(\ell)$ associated with 2-CML-PL and the experimental SLC response are similar, even though the CML was calibrated against the experimental $\varepsilon_{max}(\ell)$ and not $g_{max}(\ell)$. Furthermore, the SLC response associated with the 2-CML-PL relation overestimates the experimental SLC response for any value of the bonded length ℓ. Similarly, the slip capacities obtained from the other X_CML relations overestimate the experimental $g_{max}(\ell)$.

Among the CMLs calibrated against the $\varepsilon_{max}(\ell)$ responses with $\tau_f = 0.03$ MPa, 1_CML-PL-τ3 (Eq. (3)) provided the best results. In fact, for 1_CML-PL-τ3 the parameter $E_\varepsilon(\mathbf{p})$ is equal to 0.054, which is the lowest value of all X_CML-PL-τ3 equations. Nonetheless, very similar CMLs and values of $E_\varepsilon(\mathbf{p})$ were obtained with all X-CML-τ3 equations, as shown in Table 3. The plots of the 1_CML-PL-τ3 relation and the corresponding SC and SLC responses are shown in Fig. 6. Comparison of 1_CML-PL and 1_CML-PL-τ3 and of 2_CML-PL and 2_CML-PL-τ3 (Fig. 5b) shows that the assumption $\tau_f = 0.03$ MPa modifies the shape of the CML. In fact, when the friction shear stress is assumed equal to 0.03 MPa, the 1_ and 2_ CMLs-PL-τ3 obtained by fitting the experimental strain capacity response are comprised of an almost-linear descending branch followed by the constant branch corresponding to $\tau_f = 0.03$ MPa. This does not occur for the 3_ and 4_CML-PL-τ3 responses since these equations are derived from the equation proposed in [49,50], which entails for shear stress equal to zero at $s = 0$ and maximum shear stress at slip $s = \ln 2/\alpha$ for any A and α positive (Section 4). 1_CML-τ3 provides good results in terms of approximating the SC responses, as can be observed in Fig. 6b (2-CML-τ3 provides very similar results). This observation suggests that the adoption of a simplified CML, comprised by a linear descending branch followed by a constant branch only, could be sufficient to describe the fiber-matrix debonding with reasonable accuracy. Interestingly, the 1_CML-PL-τ3 relation does not provide the best result in terms of reproducing the load responses $P(g)$ of the m specimens. In fact, the average error $E_P(\mathbf{p})$ associated with this relation is 12.862, while the minimum average error associated with the X-CML-PL-τ3 equations is 10.024, corresponding to the 3_CML-PL-τ3 equation. It is worth noting that the error $E_\varepsilon(\mathbf{p})$ associated with 3_CML-PL-τ3 is 0.066, which is the maximum among values of $E_\varepsilon(\mathbf{p})$ of the X_CML-PL-τ3 equations. The plots of the 3_CML-
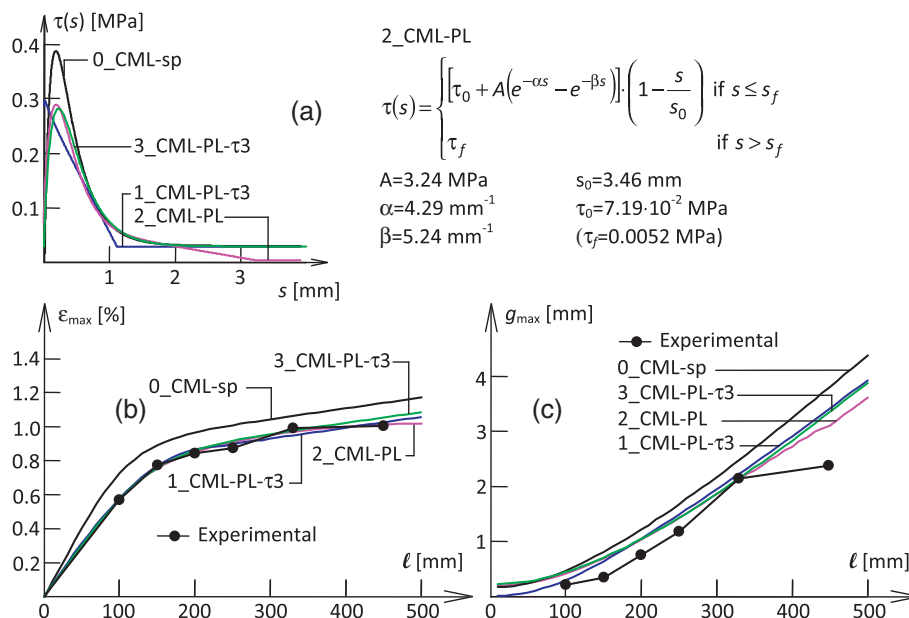
Fig. 6. (a) Comparison of the 2_CML-PL, 1_CML-PL-τ3, and 3_CML-PL-τ3 relations. (b) Comparison of the SC responses resulting from the 2_CML-PL, 1_CML-PL-τ3, and 3_CML-PL-τ3 relations and the experimental data. (c) Comparison of the SLC responses resulting from the 2_CML-PL, 1_CML-PL-τ3, and 3_CML-PL-τ3 and the experimental data.

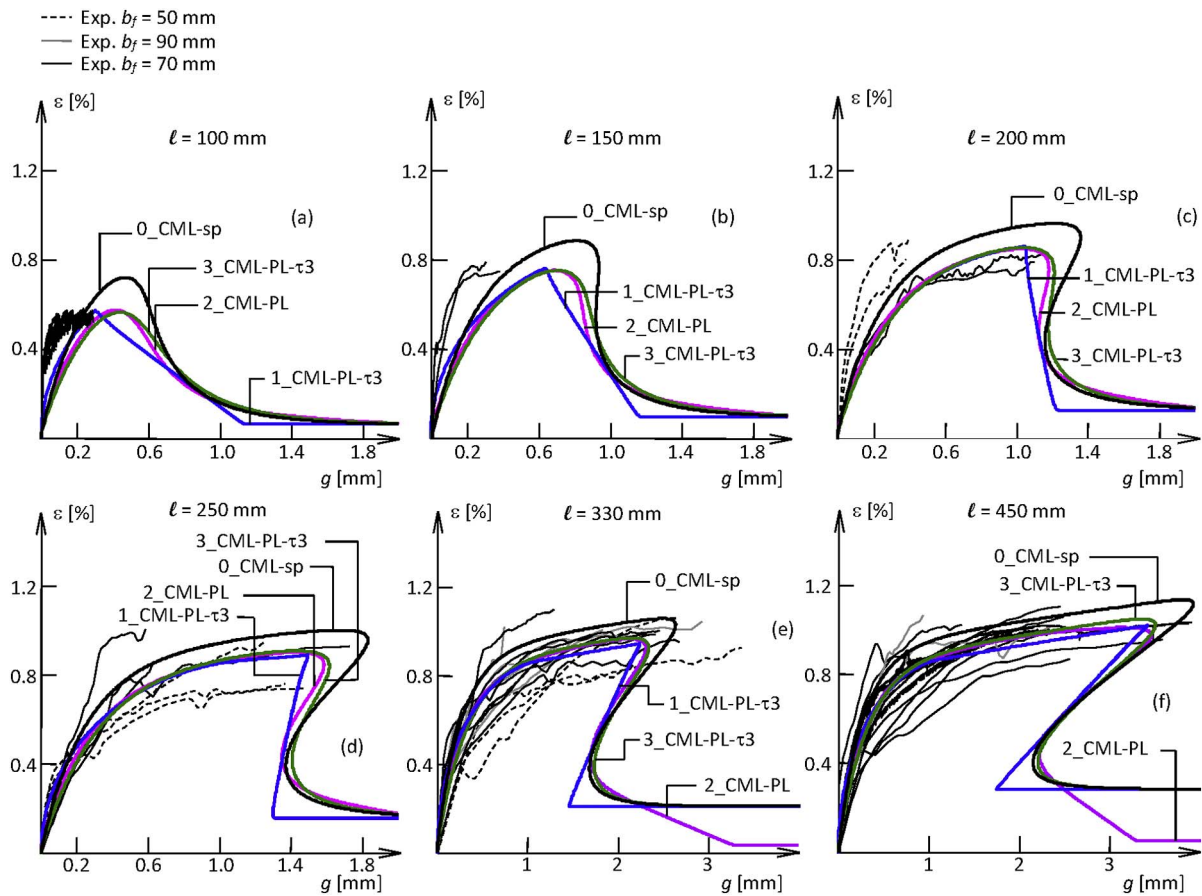**Fig. 7.** (a)–(f) Comparison between the load responses resulting from the 2_CML-PL, 1_CML-PL-τ3, and 3_CML-PL-τ3 relations relative to bonded lengths ℓ = 100, 150, 200, 250, 330, and 450 mm, respectively, and the experimental results. The load responses are expressed in terms of strain, $\varepsilon(g) = P(g)/(E_f A_f)$.

PL-τ3 and the corresponding SC and SLC responses are shown in Fig. 6. Differences between the experimental and analytical curves depicted in Fig. 6c are attributed to the experimental uncertainties. The indirect calibration method proposed does not take into account experimental uncertainties, such as the non-perfect alignment of the fibers along the longitudinal (loading) direction, and the presence of out-of-plane stresses associated with the single-lap direct-shear test set-up employed [47], but assumes the fibers are perfectly aligned and that a pure Mode-II loading condition exists.

Fig. 7 compares the load responses associated with the 0_CML-sp, 2_CML-PL, 1_CML-PL-τ3, and 3_CML-PL-τ3 relations (shown in Fig. 6a) and the ascending portion of the experimental load responses. In Fig. 7, the load responses $P(g)$ are expressed in terms of fiber strain $\varepsilon(g) = P(g)/(E_f A_f)$ to include the experimental responses of specimens with different bonded widths. Separate plots are provided for different bonded lengths. Since the experimental tests described in Section 3 were conducted by constantly increasing the global slip g, the snap-back phenomenon observed in the analytical load responses was not captured by the experimental tests. Nevertheless, the analytical load responses are plotted until a constant applied load due to friction is attained, which allowed to observe the snap-back phenomenon and the residual applied load due to friction. Furthermore, it should be noted that the descending branch of the load responses does not correspond to the descending branch of the CML. In fact, the descending (softening) branch of the CML is associated with the ascending non-linear branch of the load responses depicted in Fig. 7.

Although the shape of 1_CML-PL-τ3 is considerably different from the shape of the other CMLs in Fig. 6, the ascending branch of the load responses associated with 1_CML-PL-τ3 is similar to the ascending branch of the load responses associated with the other CMLs. Signifi-

cant differences can be observed between the descending branches of the load responses associated with the 1_CML-PL-τ3 and those associated with the other CMLs. Similar considerations could be outlined for the 2_CML-PL-τ3 relation (not shown in Fig. 7), whose shape is very similar to the shape of the 1_CML-PL-τ3 relation. Furthermore, all CMLs calibrated against the SC response are in good agreement with the experimental load responses for long bonded lengths (i.e., ℓ = 250 mm, ℓ = 330 mm, and ℓ = 450 mm), while they overestimate the global slip g associated with short bonded lengths. The load responses associated with the CML calibrated against the strain profiles (0_CML_sp) also provides results in good agreement with the experimental results for long bonded lengths, while it overestimates the capacity of the specimens with short bonded lengths.

7. Conclusions

In this paper, an indirect method to calibrate the cohesive material law (CML) of FRCM-concrete joints was proposed. The indirect calibration procedure proposed requires that single-lap shear tests are conducted on FRCM-concrete joints with different bonded lengths. The peak load versus bonded length plot was used in this paper to calibrate the CML. The procedure was successfully applied to the experimental data published in [35,36]. Five CMLs were selected and calibrated, which allowed for investigating the effectiveness of the proposed procedure without assuming a unique shape of the CML. The CML curves obtained were very similar to one another and are also similar to the average CML obtained directly from the strain profiles in [35,36]. This indicates that, for the experimental results and analytical CMLs considered, the proposed indirect calibration method provides reliable results without being affected by the particular shape of the CML

adopted. Finally, the CMLs were able to predict accurately the experimental load responses.

The following steps should be followed to apply the method proposed:

1) Select the experimental data of specimens with several bonded lengths. The failure mode must be the same among the specimens, i.e. debonding occurs at the same interface.
2) Disregard those specimens that present an uneven load distribution among the longitudinal bundles of the textile. If the shear test is equipped with at least two LVDTs that measure the slip at the loaded end, a simple calculation to verify the load distribution among the bundles was previously proposed by the authors [36].
3) Select one or more shapes of the CML. In this paper, five different expressions of the CML were considered.
4) Use the fundamental differential equation that describes the fracture mechanics Mode-II interfacial debonding to derive analytically or numerically the plot of the peak load versus bonded length from the expression of the CML.
5) Define a calibration criterion to obtain the parameters of the CML. In this paper, the calibration of the parameters of the CML was performed by adopting the non-linear least squares method.
6) Determine the parameters of the CML by best fitting the experimental data as per the calibration criterion.

The main advantage of the indirect method herein presented is that it does not require complicated or advanced equipment to measure the strain along the bonded area. After preliminary tests are performed to evaluate the fiber elastic modulus, the only experimental data required are values of the peak load for specimens with different bonded lengths. Furthermore, this method can be applied to other failure interfaces where strain measuring can be particularly challenging, such as the matrix-support interface or the internal-external matrix layer interface.

When the CML associated with a particular interface is defined by the proposed indirect calibration method, it can be employed to obtain the corresponding load response for any bonded length, which in turn provides values of peak load and corresponding slip. Furthermore, the CML obtained can be employed in numerical (FEM) or analytical models to predict the structural behavior of structural members (e.g. it can be used to obtain cracks spacing and opening of FRCM strengthened elements subjected to bending).

References

[1] S. Hashemi, R. Al-Mahaidi, Experimental and finite element analysis of flexural behavior of FRP-strengthened RC beams using cement-based adhesives, Constr. Build. Mater. 26 (2012) 268–273.

[2] H.M. Elsanadedy, T.H. Almusallam, S.H. Alsayed, Y.A. Al-Salloum, Flexural strengthening of RC beams using textile reinforced mortar - experimental and numerical study, Compos. Struct. 97 (2013) 40–55.

[3] S. Weiland, R. Ortlepp, M. Curbach, Strengthening of preformed slabs with textile reinforced concrete, Proc., 2nd International Fib Congress, Naples, Italy, 2006.

[4] A. Wiberg, Strengthening of Concrete Beams Using Cementitious Carbon Fibre Composites. Doctoral Thesis. Royal Institute of Technology, Springer, Berlin, 2003.

[5] B. Täljsten, T. Blanksvärd, Mineral-based bonding of carbon FRP to strengthen concrete structures, J. Compos. Constr. 11 (2) (2007) 120–128.

[6] L. Ombres, Flexural analysis of reinforced concrete beams strengthened with a cement based high strength composite material, Compos. Struct. 94 (1) (2011) 143–155.

[7] L. Ombres, Debonding analysis of reinforced concrete beams strengthened with fibre reinforced cementitious mortar, Eng. Fract. Mech. 81 (2012) 94–109.

[8] G. Loreto, L. Leardini, D. Arboleda, A. Nanni, Performance of RC slab-type elements strengthened with fabric-reinforced cementitious-matrix composites, J. Compos. Constr. 18 (3) (2014).

[9] S. Babaeidarabad, G. Loreto, A. Nanni, Flexural strengthening of RC beams with an externally bonded fabric-reinforced cementitious matrix, J. Compos. Constr. 18 (5) (2014).

[10] A. Brückner, R. Ortlepp, M. Curbach, Textile reinforced concrete for strengthening in bending and shear, Mater. Struct. 39 (2006) 741–748.

[11] T.C. Triantafillou, C.G. Papanicolaou, Shear strengthening of reinforced concrete members with textile reinforced mortar (TRM) jackets, Mater. Struct. 39 (2006) 93–103, http://dx.doi.org/10.1617/s11527-005-9034-3.

[12] T. Blanksvärd, B. Täljsten, A. Carolin, Shear strengthening of concrete structures with the use of mineral-based composites, J. Compos. Constr. 13 (1) (2009) 25–34.

[13] E. Tzoura, T.C. Triantafillou, Shear strengthening of reinforced concrete T-beams under cyclic loading with TRM or FRP jackets, Mater. Struct. (2014), http://dx.doi.org/10.1617/s11527-014-0470-9.

[14] C. Escrig, L. Gil, E. Bernat-Maso, F. Puigvert, Experimental and analytical study of reinforced concrete beams shear strengthened with different types of textile-reinforced mortar, Constr. Build. Mater. 83 (2015) 248–260.

[15] L. Ombres, Structural performances of reinforced concrete beams strengthened in shear with a cement based fiber composite material, Compos. Part B Eng. 122 (2015) 316–329.

[16] Z.C. Tetta, N.K. Lampros, D.A. Bournas, Textile-reinforced mortar (TRM) versus fiber-reinforced polymers (FRP) in shear strengthening of concrete beams, Compos. Part B Eng. 77 (2015) 338–348.

[17] G. Loreto, S. Babaeidarabad, L. Leardini, A. Nanni, RC beams shear-strengthened with fabric-reinforced-cementitious-matrix (FRCM) composite, Int. J. Adv. Struct. Eng. 7 (4) (2015) 341–352.

[18] T. Trapko, Fiber reinforced cementitious matrix confined concrete elements, Mater. Des. 44 (2013) 382–391.

[19] L. Ombres, Concrete confinement with a cement based high strength composite material, Compos. Struct. 109 (2014) 294–304.

[20] C.G. Papanicolaou, T.C. Triantafillou, K. Karlos, M. Papathanasiou, Textile-reinforced mortar (TRM) versus FRP as strengthening material of URM walls: in-plane cyclic loading, Mater. Struct. 40 (2007) 1081–1097, http://dx.doi.org/10.1617/s11527-006-9207-8.

[21] M. Corradi, A. Borri, G. Castori, R. Sisti, Shear strengthening of wall panels through jacketing with cement mortar reinforced by GFRP grids, Compos. Part B 64 (2014) 33–42.

[22] M.R. Valluzzi, F. Daporto, E. Garbin, M. Panizza, Out-of-plane behavior of infill masonry panels strengthened with composite materials, Mater. Struct. 47 (2014) 2131–2145.

[23] S. Babaeidarabad, F. De Caso, A. Nanni, URM walls strengthened with fabric-reinforced cementitious matrix composite subjected to diagonal compression, J. Compos. Constr. 18 (2) (2013).

[24] S. Babaeidarabad, F. Caso, A. Nanni, Out-of-plane behavior of URM walls strengthened with fabric-reinforced cementitious matrix composite, J. Compos. Constr. 18 (4) (2013).

[25] V. Alecci, F. Focacci, L. Rovero, G. Stipo, M. De Stefano, Extrados strengthening of brick masonry arches with PBO-FRCM composites: experimental and analytical investigations, Compos. Struct. 149 (1) (2016) 184–196.

[26] V. Giamundo, G.P. Lignola, G. Maddaloni, A. Balsamo, A. Prota, G. Manfredi, Experimental investigation of the seismic performances of IMG reinforcement on curved masonry elements, Compos. Part B 70 (2015) 53–63.

[27] V. Giamundo, G.P. Lignola, G. Maddaloni, F. da Porto, A. Prota, G. Manfredi, Shaking table tests on a full-scale unreinforced and IMG-retrofitted clay brick masonry barrel vault, Bull. Earthq. Eng. 14 (6) (2016) 1663–1693.

[28] G. Ramaglia, G.P. Lignola, A. Balsamo, A. Prota, G. Manfredi, Seismic strengthening of masonry vaults with abutments using Textile Reinforced Mortar, J. Compos. Constr. (2017) (in press), http://dx.doi.org/10.1061/(ASCE)CC.1943-5614.000073.

[29] L. Bednarz, A. Gorski, J. Jasienko, E. Rusinski, Simulations and analyses of arched brick structures, Autom. Constr. 20 (12) (2011) 741–754.

[30] Ł. Hojdys, P. Krajewski, Laboratory tests on masonry vaults with backfill strengthened at the extrados, Key Eng. Mater. 624 (2015) 510–517.

[31] G. De Felice, S. De Santis, L. Garmendia, B. Ghiassi, P. Larrinaga, P.B. Lourenco, D.V. Oliveira, F. Paolacci, C.G. Papanicolaou, Mortar-based systems for externally bonded strengthening of masonry, Mater. Struct. 47 (2014) 2021–2037.

[32] F.G. Carozzi, C. Poggi, Mechanical properties and debonding strength of Fabric Reinforced Cementitious Matrix (FRCM) systems for masonry strengthening, Compos. Part B 70 (2015) 215–230.

[33] C. Carloni, S. Verre, L.H. Sneed, L. Ombres, Loading rate effect on the debonding phenomenon in fiber reinforced cementitious matrix-concrete joints, Compos. Part B 108 (2017) 301–314.

[34] L.H. Sneed, T. D'Antino, C. Carloni, Investigation of bond behavior of PBO fiber-reinforced cementitious matrix composite-concrete Interface, ACI Mater. J. 111 (5) (2014) 569–580.

[35] T. D'Antino, C. Carloni, L.H. Sneed, C. Pellegrino, Matrix-fiber bond behavior in PBO FRCM composites: a fracture mechanics approach, Eng. Fract. Mech. 117 (02) (2014) 94–111.

[36] C. Carloni, T. D'Antino, L. Sneed, C. Pellegrino, Role of the matrix layers in the stress transfer mechanism of FRCM composites bonded to a concrete substrate, J. Eng. Mech. (2014), http://dx.doi.org/10.1061/(ASCE)EM.1943-7889.0000883 (04014165).

[37] A. D'Ambrisi, L. Feo, F. Focacci, Bond-slip relations for PBO-FRCM materials externally bonded to concrete, Compos. Part B 43 (8) (2012) 2938–2949.

[38] L.H. Sneed, T. D'Antino, C. Carloni, C. Pellegrino, A comparison of the bond behavior of PBO-FRCM composites determined by single-lap and double-lap shear tests, Cem. Concr. Compos. 64 (2015) 37–48.

[39] P. Foraboschi, Analytical model to predict the lifetime of concrete members externally reinforced with FRP, Theor. Appl. Fract. Mech. 75 (1) (2015) 137–145.

[40] P. Foraboschi, Predictive multiscale model of delayed debonding for concrete members with adhesively bonded external reinforcement, Compos. Mech. Comput. Appl. 3 (4) (2012) 307–329.

[41] P. Foraboschi, Effectiveness of novel methods to increase the FRP-masonry bond capacity, Compos. Part B 107 (2016) 214–232.

[42] P. Foraboschi, A. Vanin, New methods for bonding FRP strips onto masonry

structures: experimental results and analytical evaluations, Compos. Mech. Comput. Appl. 4 (1) (2013) 1–23.

[43] F. Focacci, C. Carloni, Periodic variation of the transferable load at the FRP-masonry interface, Compos. Struct. 129 (2015) 90–100.

[44] C. Carloni, F. Focacci, FRP-masonry interfacial debonding: an energy balance approach to determine the influence of the mortar joints, Eur. J. Mech. A. Solids 55 (2016) 122–133.

[45] H. Yuan, J.G. Teng, R. Seracino, Z.S. Wu, J. Yao, Full-range behavior of FRP-to-concrete bonded joints, Eng. Struct. 26 (2004) 553–565.

[46] B. Ghiassi, J. Xavier, D.V. Oliveira, P.B. Lourenço, Application of digital image correlation in investigating the bond between FRP and masonry, Compos. Struct. 106 (2013) 340–349.

[47] T. D'Antino, L.H. Sneed, C. Carloni, C. Pellegrino, Effect of the inherent eccentricity in single-lap direct-shear tests of PBO FRCM-concrete joints, Compos. Struct. 142 (2016) 117–129.

[48] E. Benvenuti, N. Orlando, D. Ferretti, A. Tralli, A new 3D experimentally consistent XFEM to simulate delamination in FRP-reinforced concrete, Compos. Part B 91 (2016) 346–360.

[49] J.G. Dai, T. Ueda, Y. Sato, Development of the nonlinear bond stress-slip model of fiber reinforced plastics sheet-concrete interfaces with a simple method, J. Compos. Constr. 9 (1) (2005) 52–62.

[50] J.G. Dai, T. Ueda, Y. Sato, Unified analytical approaches for determining shear bond characteristics of FRP-concrete interfaces through pullout tests, J. Adv. Concr. Technol. 4 (2006) 133–145.